Engineering Journal issn: 0125-8281

Article

Design and Validation of Flight Dynamics System

Sittiporn Channumsin[1,a,*], **Seksan Jaturut**[1,b], **Prakasit Udomthanatheera**[1,c], **Keerati Puttasuwan**[1,d], **Chotika Kositratpatcharasuk**[1,e], **Pitcharporn Amprai**[1,f] **and Manop Aorpimai**[2,g]

1 Geo-Informatics and Space Technology Development Agency (Public Organization): GISTDA, 88 M. 9 Thung Sukala Siracha Chonburi 20230, Thailand
2 Thaipat Satellite Research Center, Mahanakorn University of Technology, 140 Chuam Sampan Road, Nong Chok, Bangkok 105301, Thailand
*E-mail: [a]sittiporn@gistda.or.th (Corresponding author), [b]seksan@gistda.or.th, [c]prakasit.u@gistda.or.th, [d]keerati.p@gistda.or.th, [e]chotika@gistda.or.th, [f]pitcharporn@gistda.or.th, [g]manop@mut.ac.th

Abstract. This paper presents the architecture design of flight dynamics system (FDS) known as "EMERALD" developed by Geo-Informatics and Space Technology Development Agency (GISTDA) and Mahanakorn University of Technology (MUT). The capability of the system enables to provide the state vector of a satellite, mission analysis, orbit events and mission monitoring. The methodologies of orbit determination and event prediction modules implemented for mission management are presented and the validation is performed by comparing the prediction results with the performance of the mission operation. As a result of the implementation, the reduction of the operation time consumption is improved significantly and the prediction performance is high accurate and reliable when comparing with previous FDS (Quartz) developed by EADS ASTRIUM.

Keywords: Validation, Thaichote satellite, orbit control, flight dynamics software, EMERALD, graphic user interface, orbit analysis tool, mission analysis, station keeping.

ENGINEERING JOURNAL Volume 23 Issue 2
Received 15 March 2018
Accepted 4 January 2019
Published 31 March 2019
Online at http://www.engj.org/
DOI:10.4186/ej.2019.23.2.97

1. Introduction

The flight dynamics system (FDS) has proven as a one of essential elements in the satellite ground control for mission planning and analysis. The FDS receives the mission requirement and information of orbital conditions to provide the orbit analysis to fulfill mission objectives. The FDS acts as an information hub for the ground control systems as shown in Fig. 1. FDS receives GPS data from satellite control center (SCC) and uses this information to returns orbital position known as "ephemeris" to mission planning center (MCC) and forecasted events (pass schedule and maneuver information) to SCC. Based on operation experiences of Thaichote (Thailand Earth observation mission) by Geo-Informatics and Space Technology Development Agency (GISTDA), the original FDS is dependent on machine and complex system to adjust and develop new features for the new requirements of future missions (e.g. multi-mission ground segment). The FDS costs of private satellite technology companies (e.g. Satellite tool kit (STK), FreeFlyer and FocusSuite) are expensive and require paying an annual cost. However, the payment decision is accepted but a customer needs to develop source codes for an initial set up of the software to align a format and satellite command. Besides, an additional cost will be added when new features are required. As a result, it consumes high budget in each year for the current and future mission operations. To reduce the budget in long-term, support the flexibility of modification and enhance technology capabilities, GISTDA researches and develops FDS to support our own mission operations as same as other international space agencies [1-3]. FDS known as "EMERALD" decided and developed by GISTDA can provide essential information of routine operations, navigation, mission design, operations of mid-term and long-term near-Earth. The graphical user interface (GUI) is developed to provide all the essential input parameters and analyzed results in a single window. Previous investigations of the authors present the high performance in the orbital trajectory tool and maneuver design [4].

This paper describes the architecture design of EMERLAD and the methodology in orbit determination and event prediction modules to compute essential information (ephemeris predictions, pass schedule and Earth eclipse) of the Thaichote mission. The analyzed results are compared with the results of previous FDS software (Quartz+) developed by EADS ASTRIUM to measure the EMERALD performance. To validate the accuracy of the EMERALD prediction, the results are compared with the mission results. Finally, the conclusion and future development are described in the last section.

2. Architecture and Design

The challenge to develop the flight dynamics technologies (algorithm, software and improvement of GUI) is the accuracy of a prediction and reliable system. The successful development allows us to upgrade the advance hardware and the software domain. EMERALD architecture is designed based on the object orientation leading to a powerful tool for development and effective cost of software maintenance. The object orientation allows us to create advanced system function, which is not only coupled with object oriented analysis for FDS in future missions but also decoupled between application and support functions. It is useful to increase the overall robustness of the system because the coding can be separated from software testing before implementing GUI by fully non-disruptive mechanism. EMERALD has been developed with the precise trajectory generation based on numerical technique and perturbations describing in section 3.

Fig. 2 shows EMERALD architecture system. The system consists of five main modules. The orbit determination and event prediction modules are main modules to support the mission operation. The orbit determination requires GPS data from a satellite to estimate the initial state vector (position and velocity), which will be an input of the event prediction module to propagate the orbital state for the prediction of the critical and mission events. The orbit control maneuver is capable of designing and planning delta-V strategies for mission performance and collision avoidance from space objects. Collision risk assessment module take responsible to analyze the collision risk of space debris or satellites and support the maneuver decision. This module is processed when we receive a notification (Conjunction Data Message: CDM) by Joint Space Operations Center (JSpOC). Finally, the de-orbit module [5] is capable of analyzing a strategy to re-entry to the Earth by performing the guidelines of Inter-Agency Debris Coordination Committee (IADC) [6] that post-mission orbit lifetime no longer than 25 years is in active regions. All analyzed results of all modules will be transferred to store in the database of the ground control system.

The FDS process of the mission operation in Fig. 3 starts when GPS decoded from telemetry are stored in database. GPS are firstly retrieved to process in the orbit determination module to estimate an initial state vector by using weighted least squares. Secondly, an initial state vector is an input for event prediction module to predict the future state vectors of a satellite and critical events. Bulirsch StÖer algorithm [6] is numerical integration technique to predict an orbital evolution under perturbations. The event prediction module provides ephemeris, pass schedule and Earth eclipse. The technique information of both modules will be described in the next section.

3. Methodology

This section describes the techniques in orbit determination, orbit propagation and algorithms to predict the critical mission event (pass schedule and Earth eclipse).

3.1. Orbit Determination

Weighted least squares technique is implemented to find the satellite trajectory by applying weighting factor to each residual in term of the square of the weighted residuals. The cost function for the weighted least squares problem is given by:

$$J = \frac{1}{2}\sum_{i=1}^{N} w_i^2 \bar{r}_i^2 = \frac{1}{2}\bar{\boldsymbol{r}}^T \boldsymbol{W}\bar{\boldsymbol{r}} = \frac{1}{2}(\boldsymbol{y}-\boldsymbol{Hx})^T \boldsymbol{W}(\boldsymbol{y}-\boldsymbol{Hx}) \tag{1}$$

where $\bar{\boldsymbol{r}}$ is the residual matrix, $\boldsymbol{W}$ is weight matrix, $\boldsymbol{y}$ is an n-dimensional vector of measurement, $\boldsymbol{H}$ donates the observation sensitivity matrix and $\boldsymbol{x}$ is the state vector matrix at the reference epoch. The necessary condition to minimize the cost function requires that the second derivative must be positive and the first derivative of the cost function equal zero:

$$\frac{\delta J}{\delta \boldsymbol{X}} = \frac{\delta(\boldsymbol{y}-\boldsymbol{Hx})^T \boldsymbol{W}(\boldsymbol{y}-\boldsymbol{Hx})}{\delta \boldsymbol{X}} = 0 \tag{2}$$

Then, Eq. (2) is rearranged to obtain the normal equation as:

$$\boldsymbol{H}^T\boldsymbol{Wy} = (\boldsymbol{H}^T\boldsymbol{WH})\boldsymbol{x} \tag{3}$$

The estimation of weight least square, $\hat{\boldsymbol{X}}$, is expresssed as:

$$\hat{\boldsymbol{X}} = \left(\boldsymbol{H}^T\boldsymbol{WH}\right)^{-1} \boldsymbol{H}^T\boldsymbol{Wy} \tag{4}$$

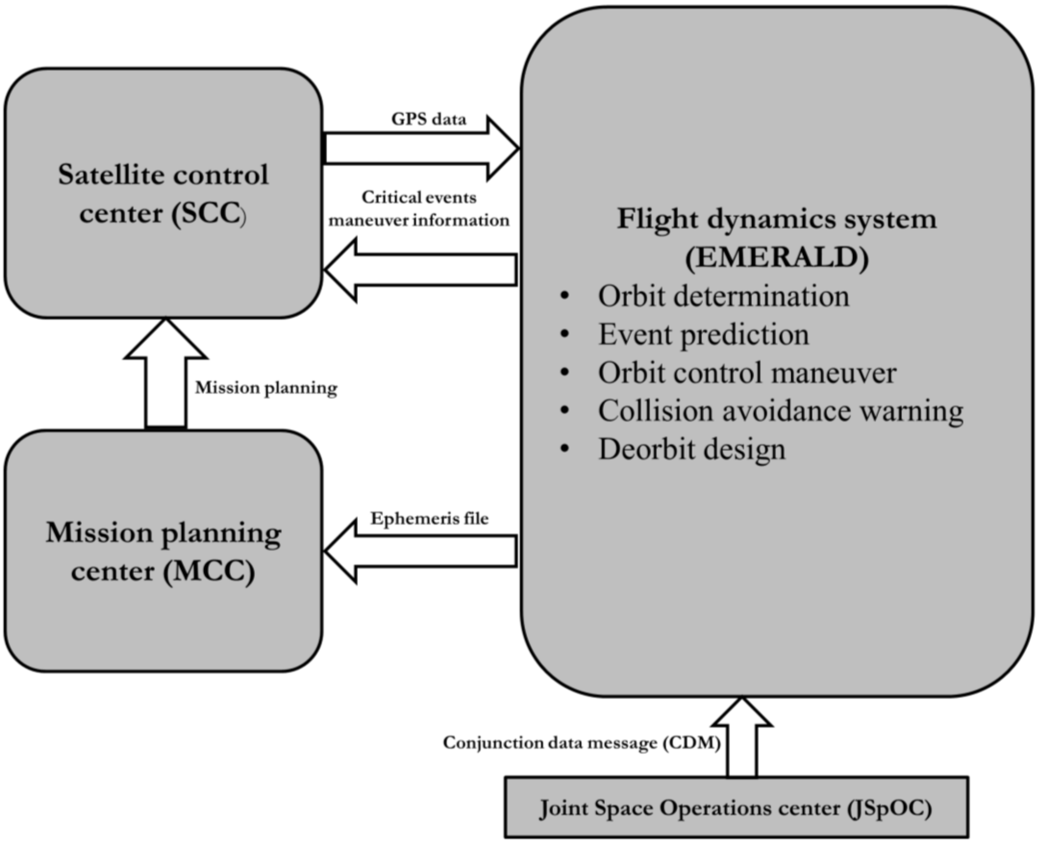

Fig. 1. Thaichote Ground control system.

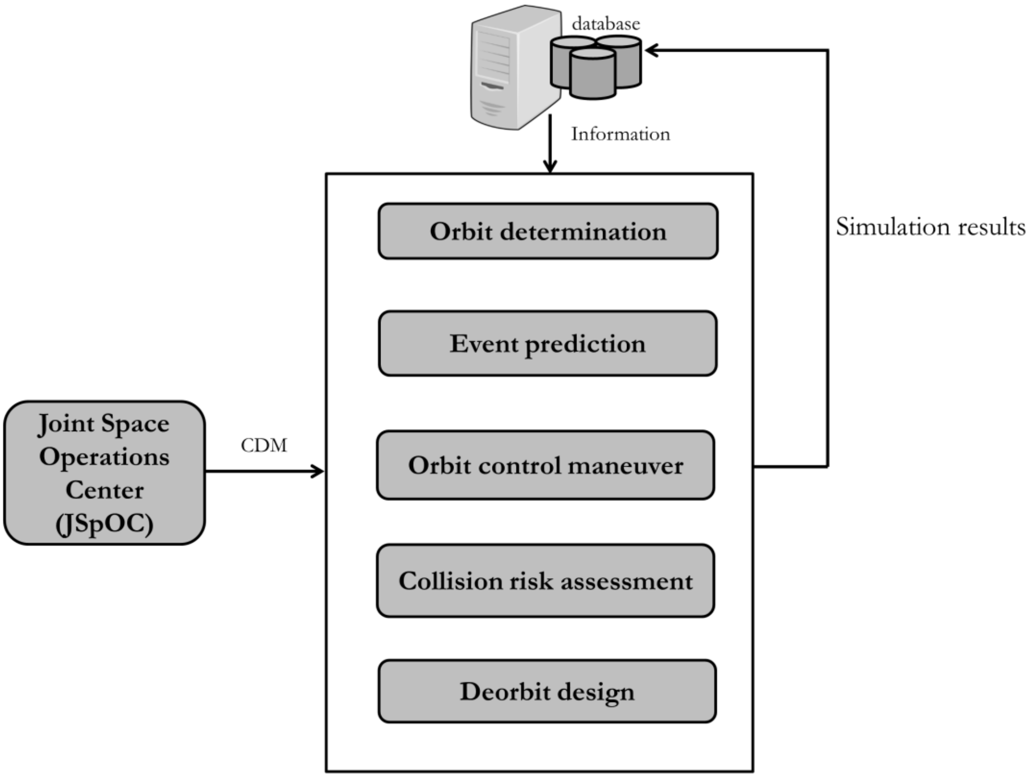

Fig. 2. EMERALD architecture.

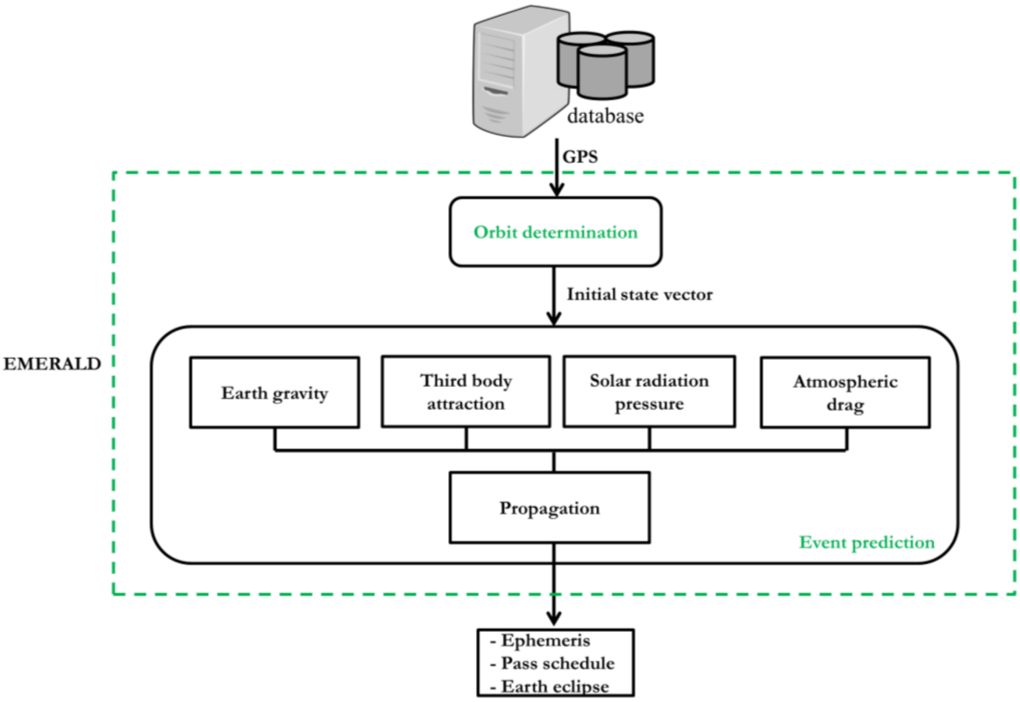

Fig. 3. Orbit determination and event prediction process.

3.2. Orbit Propagation

The perturbations acting on satellite are typically modelled by applying a gravity field from the Earth, third body gravity forces due to the Sun and Moon and may include tides, atmospheric drag, solar radiation pressure and other effects as deemed necessary. In this software, the perturbative accelerations that will be considered are: Earth gravitational field ($\vec{a}_{Earth}$), the third body gravity of Sun and Moon ($\vec{a}_{sun}, \vec{a}_{moon}$), air drag ($\vec{a}_{SRP}$) and SRP ($\vec{a}_{Drag}$). Therefore, the orbital dynamic model used for the orbit propagation is expressed as:

$$\ddot{\vec{x}}_{total} = \vec{a}_{Earth} + \vec{a}_{sun} + \vec{a}_{moon} + \vec{a}_{SRP} + \vec{a}_{Drag} \tag{5}$$

where $\ddot{\vec{x}}_{total}$ is total acceleration of satellite position.

The numerical integration used to solve the propagation of the differential equations is the Bulirsch StÖer algorithm [7] that provides high-accuracy solution to ordinary differential equations with reasonable computational efforts.

3.2.1. Two body perturbations

Newton's law of gravitation determines that every point mass attracts every single point mass by a force, which is proportional to the product of the two masses and inversely proportional to the square of the distance between them. Due to imperfect sphere of the Earth, the effect of the Earth's oblateness is considered for higher accuracy of an orbital prediction. The acceleration of the Earth gravity acting on the satellite from the Earth is written as:

$$\vec{a}_{Earth} = \nabla\left[\frac{\mu}{x}\left[1+\sum_{l=2}^{\infty}\sum_{m=0}^{l}\left(\frac{R_E}{x}\right)^{l} P_{lm}\left[\sin\phi_{sat}\right]\left\{C_{lm}\cos(m\lambda_{sat})+S_{lm}\sin(m\lambda_{sat})\right\}\right]\right] \tag{6}$$

Where x is magnitude of the position vector, μ is the gravitation constant of the Earth, R_E is the Earth's mean equatorial radius, l and m are degree and order of spherical harmonics, P_{lm} is Legendre function at l degree and m order, both C_{lm} and S_{lm} are normalized surface spherical harmonics coefficients. Finally, ϕ_{sat} and λ_{sat} are geocentric latitude and longitude of a satellite.

3.2.2. Third body perturbations

The perturbations of the Sun and the Moon in an Earth-centered reference are given by:

$$\vec{a}_k = -\sum_{k=1,2} \mu_k \left(\frac{\vec{x}-\vec{x}_k}{\left|\vec{x}-\vec{x}_k\right|^3} + \frac{\vec{x}_k}{\vec{x}_k^3} \right) \tag{7}$$

where $\vec{x}_k$ is the position vector of the third body gravitational perturbations of the Sun and Moon (*k* = 1 and 2 respectively), μ_k is the gravitational constant of third body gravitational perturbations of the Sun and Moon ($\mu_1 = 1.32712438 \times 10^{20}$ m^3/s^2 and $\mu_2 = 4.902794 \times 10^{12}$ m^3/s^2 respectively).

3.2.3. Solar radiation pressure

The satellite is assumed to be a spherical body with uniform reflection properties called "cannonball model" [8]. The direct radiation acceleration is given by:

$$\vec{a}_{SRP} = -\frac{E}{c}(1 + C_R \frac{4}{9})\frac{A}{m}\hat{\vec{S}} \tag{8}$$

where E is the solar flux (1,353 W/m^2), c is velocity of light (299,792,458 m/s), C_R is reflection coefficients, A is cross-section area of a satellite, m is a mass of satellite and $\hat{\vec{S}}$ is the unit vector pointing from the satellite to the Sun.

3.2.4. Atmospheric drag

In low Earth orbit (LEO), the effects of atmospheric perturbation is essential to be considered for more accuracy the orbital propagation. The aerodynamic acceleration [9] acting on a satellite in orbit is given by:

$$\vec{a}_{drag} = -\frac{1}{2} C_d \frac{S}{m} \rho V_{rel}^2 \hat{\vec{V}}_{rel} \tag{9}$$

where S is the cross-section area of the main body perpendicular a relative velocity unit vector to the rotating atmosphere ($\hat{\vec{V}}_{rel}$), C_d is the drag coefficient of a satellite and ρ is atmosphere density depending on the satellite altitude.

3.3. Rise/Set Time

A satellite can contact a ground station when it rises above a minimum elevation angle. Let θ denote the elevation angle.

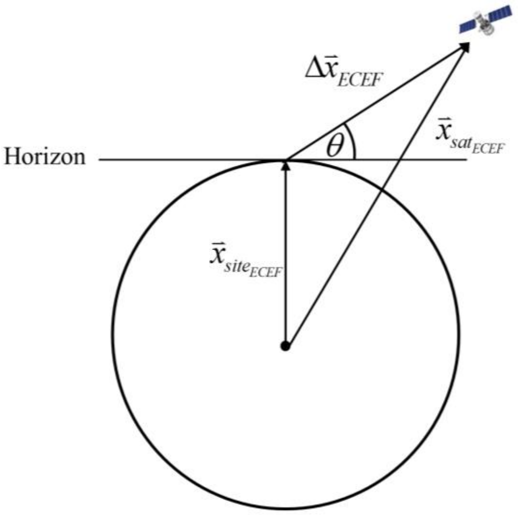

Fig. 4. Geometry of Rise/set time.

In Fig. 4, the angle (θ) shows between the vector of the ground target ($\vec{x}_{site_{ECEF}}$) and relative vector ($\Delta\vec{x}_{ECEF}$). The elevation angle is measured from the horizon up to satellite. The angle is given by:

$$\theta = \sin^{-1}\left(\frac{\Delta\vec{x}_{ECEF}\cdot\hat{\vec{x}}_{site_{ECEF}}}{\left\|\Delta\vec{x}_{ECEF}\right\|}\right) \tag{10}$$

where $\Delta\vec{x}_{ECEF} = \vec{x}_{sat_{ECEF}} - \vec{x}_{site_{ECEF}}$, $\vec{x}_{sat_{ECEF}}$ and $\vec{x}_{site_{ECEF}}$ are the position vectors of the satellite and the ground target in the Earth centered Earth fixed frame (ECEF) respectively. The value of the right hand side in Eq. (10) varies with time that can be defined as the visibility function. Therefore, the visibility function is expressed by:

$$V(t) = \sin\theta = \frac{\Delta\vec{x}_{ECEF}\cdot\hat{\vec{x}}_{site_{ECEF}}}{\left\|\Delta\vec{x}_{ECEF}\right\|} \tag{11}$$

The elevation angle represents the zero of the function. In case of Thaichote mission (altitude: 822 km, sun synchronous orbit and a ground target location at 13.10ºN, 100.92ºE), the minimum elevation threshold is controlled at 5 degrees.

3.4. Earth Eclipse

Earth eclipse events have significant impacts on the satellite mission. It is required to know exactly when the satellite enters or leaves the shadow region because the eclipse effects the management of the satellite's energy storage, thermal control of satellite and effect of trajectory propagation of the satellite due to the solar radiation pressure that is small or null in the penumbra or umbra. In EMERALD, the conical shadow model is employed for the eclipse prediction. The penumbra (light gray) and umbra (dark gray) in Fig. 5 are demonstrated by the distance between the Sun and the Earth.

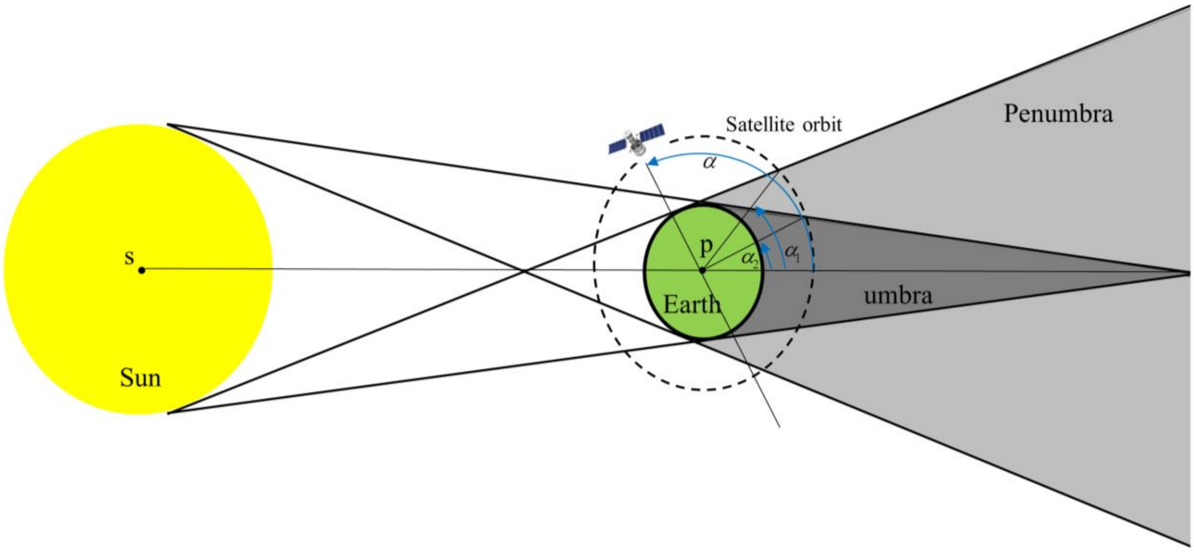

Fig. 5. Geometry of penumbra and umbra of the Earth's Eclipse.

The penumbra cone geometry is expressed as:

$$\begin{aligned} \alpha_1 &= \pi - \cos^{-1}\left(\frac{R_e}{y_1}\right) - \cos^{-1}\left(\frac{R_e}{|\vec{x}|}\right) \\ y_1 &= \frac{R_e AU}{R_s + R_e} \end{aligned} \tag{12}$$

where R_e is the radius of the Earth (6,356.8 km), R_s is the radius of the sun (698,700 km), AU is the distance between the Earth and the Sun (149,597,870.7 km). Then, the umbra cone geometry is given by:

$$\begin{aligned} \alpha_2 &= \pi - \cos^{-1}\left(\frac{R_e}{y_2}\right) - \cos^{-1}\left(\frac{R_e}{|\vec{x}|}\right) \\ y_2 &= \frac{R_e AU}{R_s - R_e} \end{aligned} \tag{13}$$

The angle can be computed as:

$$\alpha_1 = \pi - \cos^{-1}\left(\frac{\vec{x}_1 \cdot \vec{x}}{|\vec{x}_1||\vec{x}|}\right) \tag{14}$$

The satellite orbits in the penumbra region if $\alpha_2 < \alpha < \alpha_1$ while it orbits in the umbra region if $\alpha < \alpha_2$ and then in case of α is equal to α_1 or α_2. It can imply that a satellite is entering or leaving the penumbra or umbra.

4. Results and Discussion

The simulation results of the event prediction module will be compared corresponding value obtained by Quartz and the results will be shown the maximum relative error of each day. The relative error between both results will be computed by:

$$error[\%] = \frac{|value_{EMERLAD} - value_{Quartz}|}{value_{Quartz}} \times 100 \tag{15}$$

For the machine to process, Quartz is processed with a sun workstation: Sun blade 100 CPU: Sun UltraSPARC IIe 500MHz processor and 2048 MiB because this system is dependent on the machine by fixing MAC address. Then, EMERALD is run on a PC with Intel® Xeon® 3.50 GHz with 8 GB of RAM.

4.1. Ephemeris

Fig. 6–11 show the maximum relative error of six Kepler elements (semi-major axis (a), eccentricity (e), inclination (i), right accession of ascending node or RAAN (Ω), argument of perigee (ω) and true anomaly (υ)) with respect to Quartz on each day from Jun 28 to Nov 13 2017. Most of simulation trends fluctuate in small range while the RAAN trend is the smoothest between 4.53E-4 – 5.67E-4%. The statistical analysis in Table 1 indicates that the error ranges of each parameter are tiny. It can imply that the EMERALD results are high accurate with respect to Quartz. The validation is performed by comparing the coordinates of 4 corners (NW: Northwest, NE: Northeast, SW: Southwest and SE: Southeast) on an image between real coordinates based on GPS and simulated prediction of EMERALD. The control of tolerance error is equal or less 2 km within ±12° roll rotation. Table 2 shows the pointing accuracy error summary of images on July 19 and 26 2017. The errors are under control and maximum error is 0.296 km. This can imply that the orbit prediction is highly accurate.

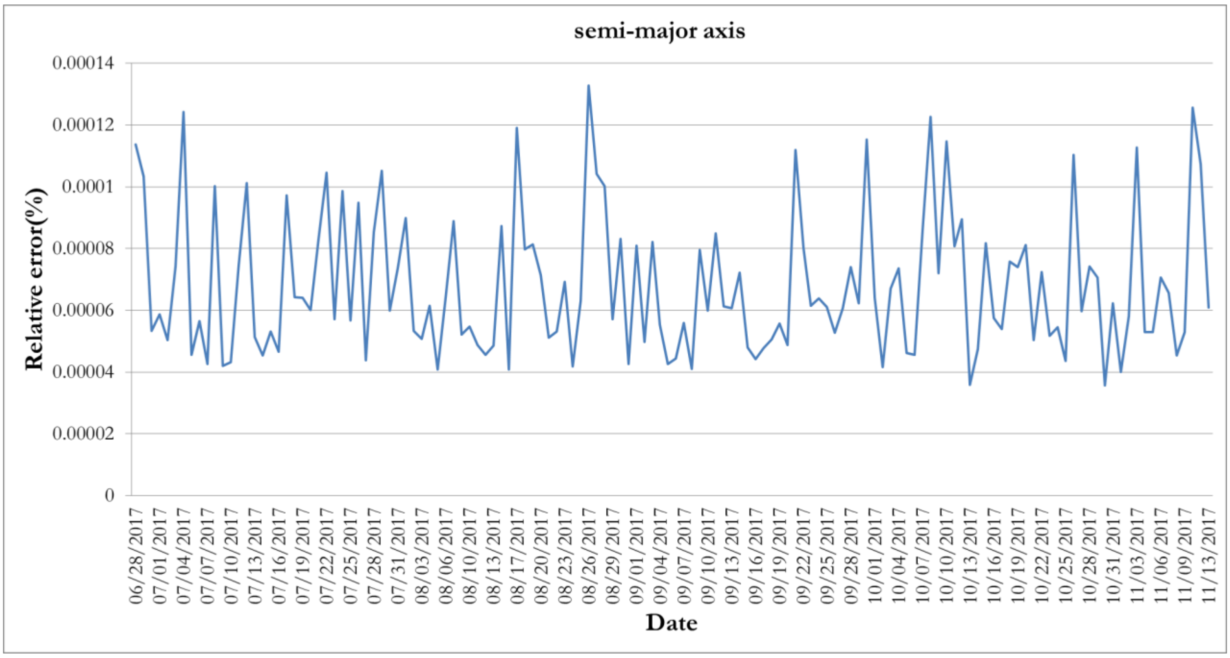

Fig. 6. Maximum relative error on each day of semi-major axis evolution on Jun 28–Nov 13 2017.

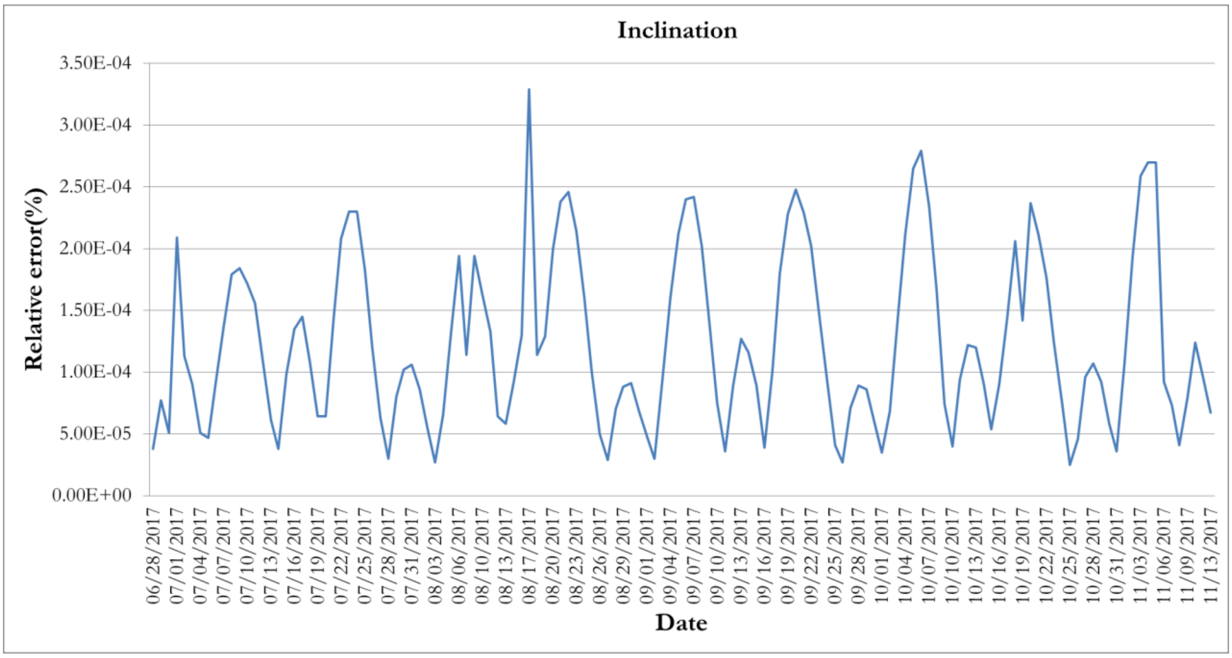

Fig. 7. Maximum relative error on each day of inclination evolution on Jun 28–Nov 13 2017.

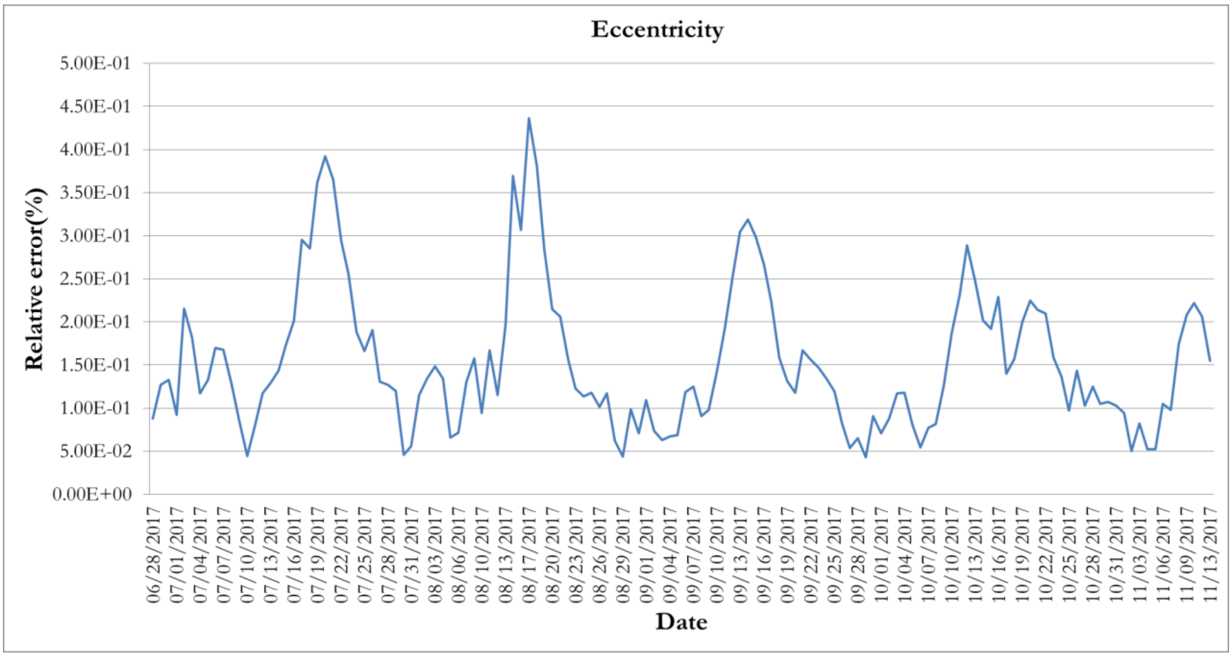

Fig. 8. Maximum relative error on each day of eccentricity evolution on Jun 28–Nov 13 2017.

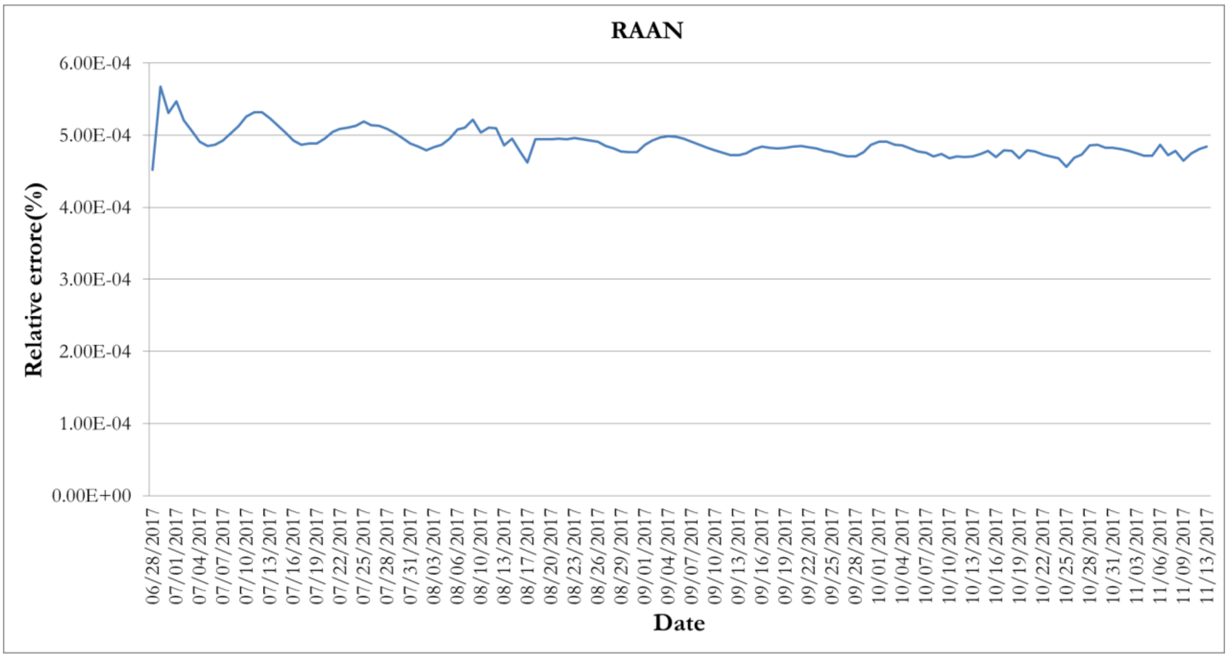

Fig. 9. Maximum relative error on each day of right ascension ascending node evolution on Jun 28–Nov 13 2017

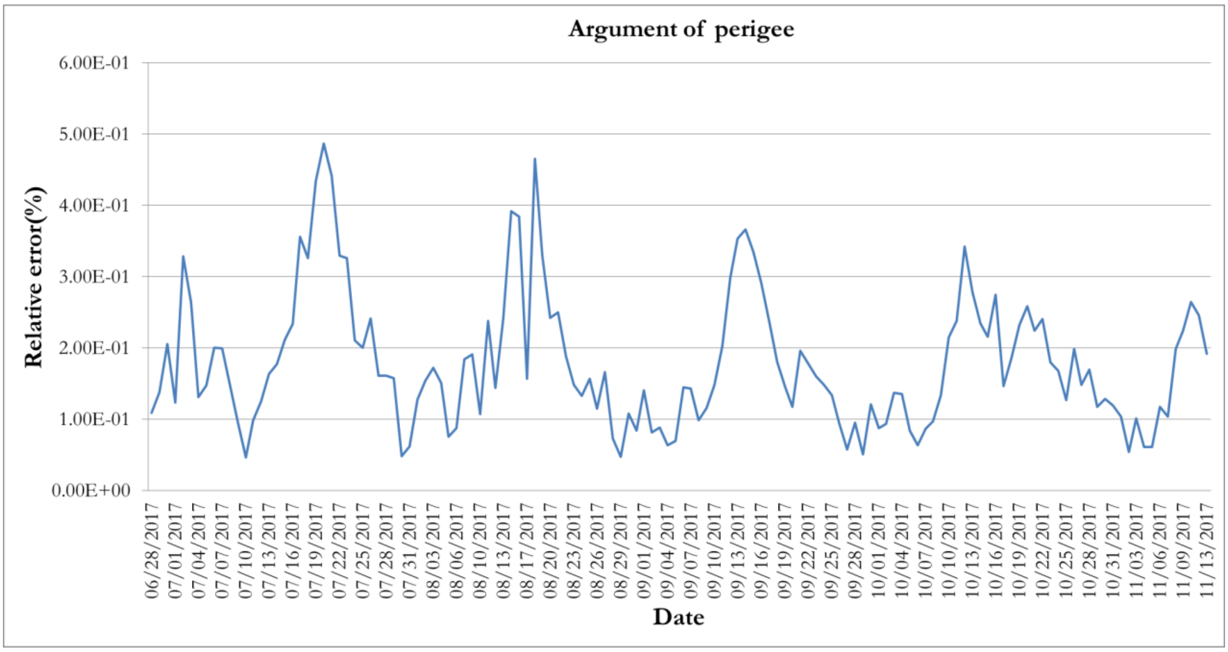

Fig. 10. Maximum relative error on each day of argument of perigee evolution on Jun 28–Nov 13 2017.

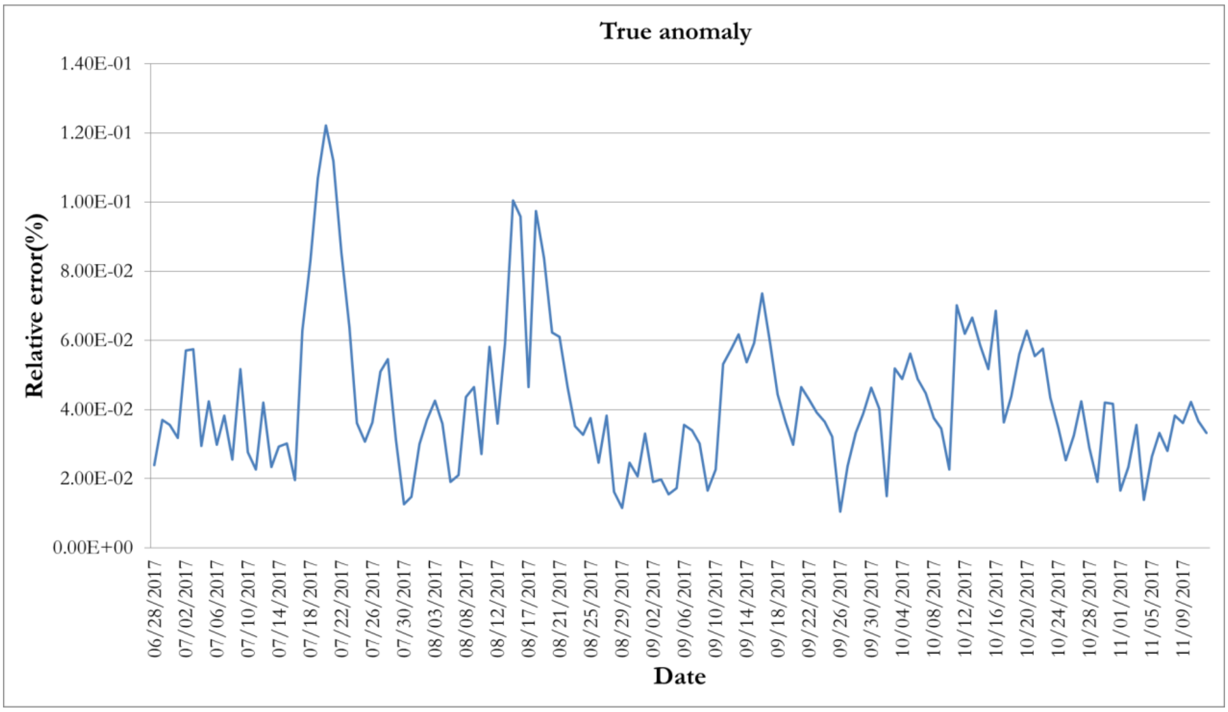

Fig. 11. Maximum relative error on each day of true anomaly evolution during Jun 28–Nov 13 2017.

Table 1. Statistical analysis of the relative difference of Kepler elements.

Elements	Maximum error	Minimum error	mean	SD
a (km)	9.57E-03	3.57E-05	0.00484738	0.00168558
e	5.06E-06	4.34E-02	0.00000179	0.00000096
i(deg)	3.29E-04	2.53E-05	0.00012365	0.00006969
Ω (deg)	1.39E-03	4.56E-04	0.00127545	0.00004677
ω (deg)	3.30E-01	5.10E-02	0.16122824	0.08469011
υ (deg)	4.40E-01	1.05E-02	0.15312075	0.07717886

Table 2. Pointing accuracy error summary on Jul 19 and 26 2017.

Image	Segment description	Date	Corner	Roll Angle (deg)	Pointing Error(km)
1	KAZ_A13_WC	19/07/2017	NW	-6.54	0.246
			NE		0.296
			SW		0.196
			SE		0.219
2	KAZ_A19_WC	19/07/2017	NW	1.71	0.208
			NE		0.189
			SW		0.235
			SE		0.158
3	Libye4_IQ	19/07/2017	NW	-2.32	0.254
			NE		0.260
			SW		0.218

			SE		0.230
4	USA_L1_12_WC	19/07/2017	NW	1.13	0.115
			NE		0.245
			SW		0.185
			SE		0.223
5	USA_L1_2_WC	26/07/2017	NW	0.37	0.232
			NE		0.216
			SW		0.202
			SE		0.232
6	KAZ_A20_WC	26/07/2017	NW	0.13	0.262
			NE		0.119
			SW		0.202
			SE		0.259
7	POL_1_WC	26/07/2017	NW	-3.96	0.104
			NE		0.205
			SW		0.104
			SE		0.204

4.2. Pass Schedule

A number of satellite passes depend on the mission orbit. Thaichote mission normally have 3-4 passes per day. The simulation results on Nov 5-6 2017 of EMERALD and Quartz are shown in Table 3. The number of pass schedules on both days are equal and the pass period difference of EMERALD prediction shown in Fig. 12 are 2 and 1 seconds on Nov 5-6 2017 respectively. The transponders on Thaichote normally turn on and off before and after pass schedule for 2.30 minutes. This implies that the small difference does not affect the mission control.

Table 3. Comparison of visibility entry and exit time of EMERALD and Quartz.

Date	**EMERALD**		**Quartz**	
	Entry	**Exit**	**Entry**	**Exit**
Nov 5 2017	2:15:37	2:25:35	2:15:37	2:25:35
	3:54:36	4:06:38	3:54:36	4:06:38
	15:01:44	15:14:44	15:01:45	15:14:43
Nov 6 2017	1:57:54	2:04:47	1:57:54	2:04:47
	3:35:04	3:47:50	3:35:05	3:47:50
	14:42:40	14:55:25	14:42:40	14:55:25
	16:25:38	16:32:41	16:25:38	16:32:41

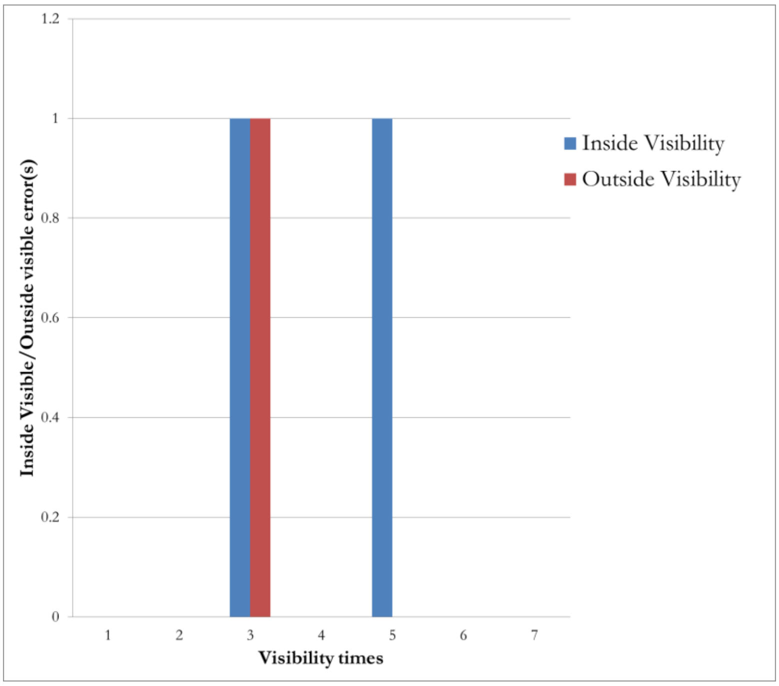

Fig. 12. Difference of inside and outside visibility time with respect to Quartz on Nov 5-6 2017.

4.3. Rise/Set Time

The maximum relative error on each day of a satellite to site visibility (elevation and azimuth) is presented in Fig. 13 and Fig. 14. In Table 4, the statistic relative error summary of both elevation and azimuth shows the narrow ranges: 0.256-0.368 % (0.231-0.332 degree) and 0.003-0.293 % (0.011-0.753 degree) respectively. The pointing errors are very tiny. The results show high precision and accuracy to predict the visibility of a satellite when comparing the capability of the antenna accuracy: 2 degrees. Time schedule and rise/ set time are information of an antenna coordinate to transmit satellite command during satellite pass. Therefore, the validation of the simulated results can be performed by measuring the radio frequency level of the satellite transmission during the pass schedule. Fig. 15 presents that the period of the radio frequency level in the 1st pass on Nov 5 2017 and 4th pass on Nov 6 2017 are good agreement as the prediction results in Fig. 15.

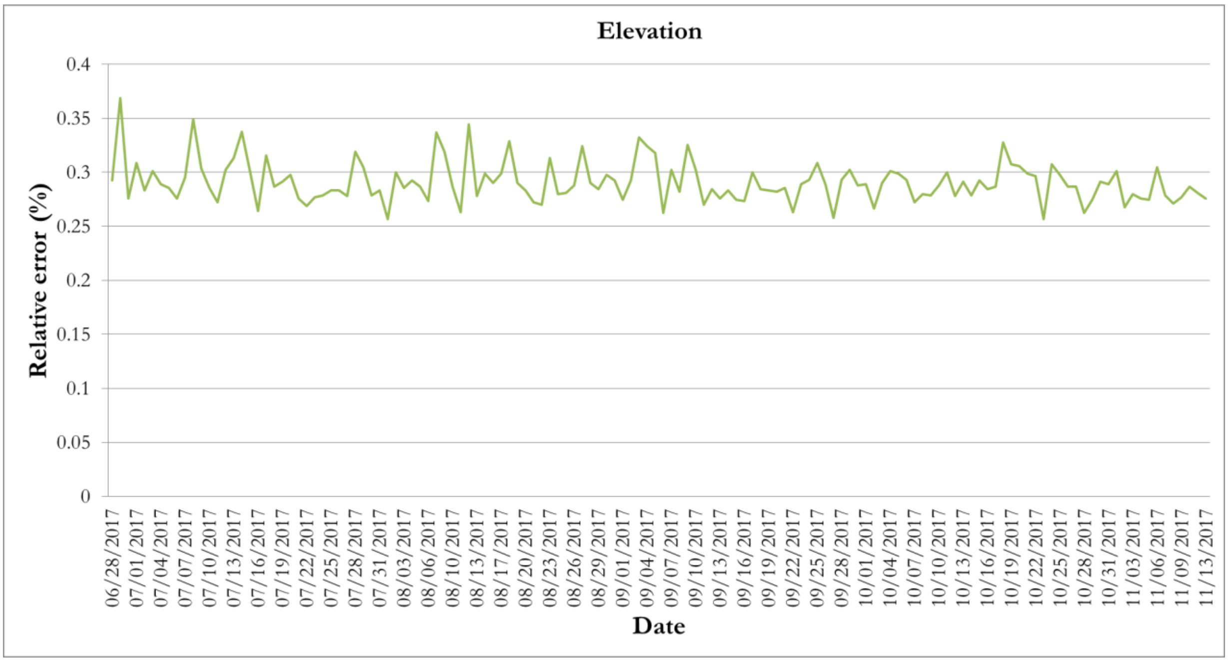

Fig. 13. Maximum relative error on each day of elevation evolution on Jun 28–Nov 13 2017.

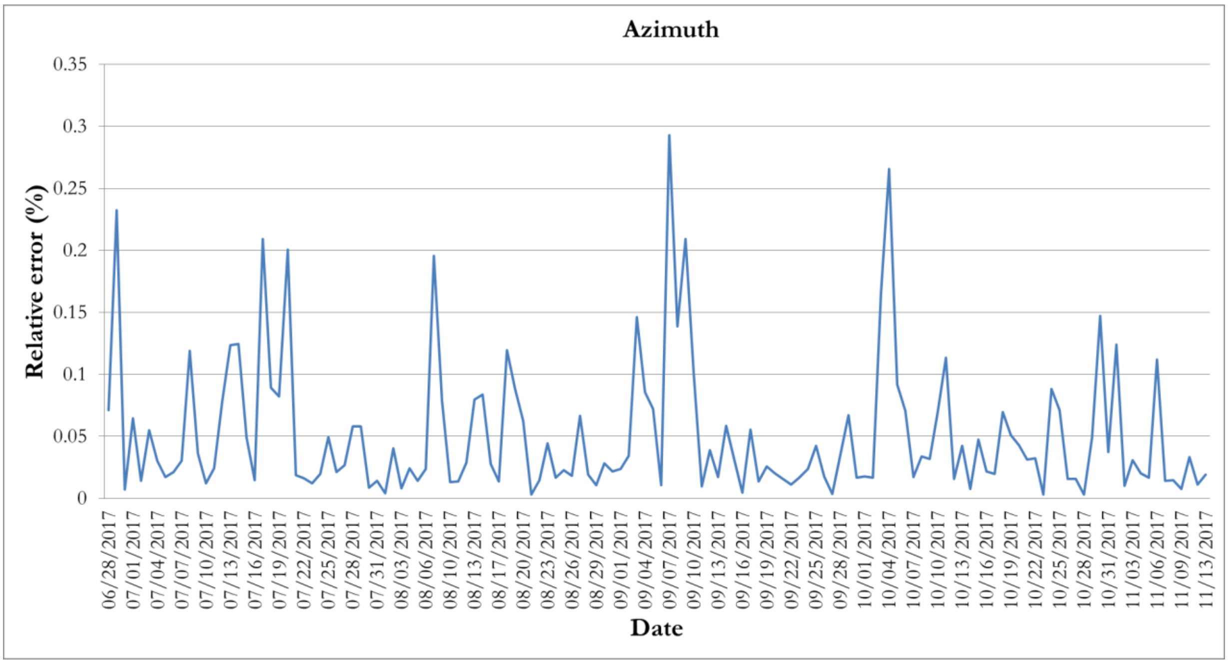

Fig. 14. Maximum relative error on each day of azimuth evolution on Jun 28–Nov 13 2017.

Table 4. Statistical analysis of the relative difference of look angles.

Parameters	Maximum	Minimum	Mean	SD
Elevation(deg)	0.332	0.231	0.261	0.017
Azimuth(deg)	0.753	0.011	0.171	0.168

a)

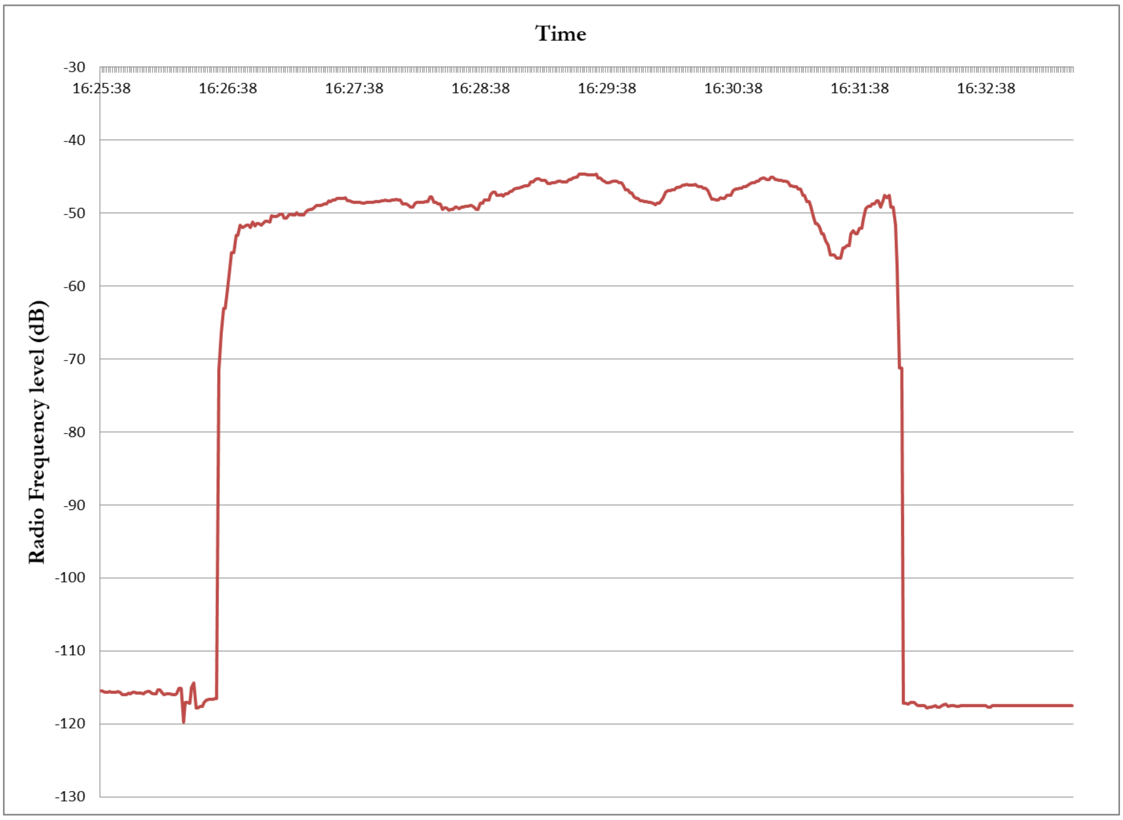

b)

Fig. 15. Radio frequency level during pass period a) 1st pass (2:15:37–2:25:35) on Nov 5 2017 b) 4th pass (14:42:40 – 14:55:25) on Nov 6 2017.

4.4. Eclipse

The comparison of the prediction results of the Earth eclipse entry and exit period on Nov 5-6 2017 is presented in Table 5. The relative differences of penumbra entry, umbra entry, umbra exit and penumbra exit with respect to Quartz are presented in Fig. 16. The differences are found only the 2nd penumbra entry and 17th umbra exit. The Earth eclipse prediction is validated by measuring the charging current profile of battery during the eclipse. Fig. 17 shows the charging current profile of the first Earth eclipse on Nov 5 2017 (1:16:31–1:49:35). The charging current starts suddenly decreasing in penumbra but there are small charging currents in penumbra and they will be zero in umbra. The charging current period therefore matches well with the Earth eclipse prediction.

Table 5. Entry and exit times of penumbra and umbra (hour: minute: second) on Nov 5-6 2017 computed by Quartz and EMERALD.

Date	**EMERALD**				**Quartz**			
	Entry		**Exit**		**Entry**		**Exit**	
	Penumbra	**Umbra**	**Umbra**	**Penumbra**	**Penumbra**	**Umbra**	**Umbra**	**Penumbra**
Nov 5 2017	1:16:31	1:16:42	1:49:24	1:49:35	1:16:31	1:16:42	1:49:24	1:49:35
	2:58:00	2:58:10	3:30:52	3:31:03	2:57:59	2:58:10	3:30:52	3:31:03
	6:01:34	6:01:45	6:34:28	6:34:38	6:01:34	6:01:45	6:34:28	6:34:38
	7:43:03	7:43:13	8:15:56	8:16:07	7:43:03	7:43:13	8:15:56	8:16:07
	9:24:31	9:24:42	9:57:25	9:57:35	9:24:31	9:24:42	9:57:25	9:57:35
	11:06:00	11:06:10	11:38:53	11:39:04	11:06:00	11:06:10	11:38:53	11:39:04
	12:47:28	12:47:38	13:20:21	13:20:32	12:47:28	12:47:38	13:20:21	13:20:32
	14:28:56	14:29:07	15:01:50	15:02:00	14:28:56	14:29:07	15:01:50	15:02:00
	16:10:25	16:10:35	16:43:18	16:43:29	16:10:25	16:10:35	16:43:18	16:43:29
	17:51:53	17:52:04	18:24:47	18:24:57	17:51:53	17:52:04	18:24:47	18:24:57
	19:33:22	19:33:32	20:06:15	20:06:26	19:33:22	19:33:32	20:06:15	20:06:26
	21:14:50	21:15:01	21:47:44	21:47:54	21:14:50	21:15:01	21:47:44	21:47:54
	21:34:12	21:34:23	22:07:06	22:07:16	21:34:12	21:34:23	22:07:06	22:07:16
	23:15:41	23:15:51	23:48:34	23:48:44	23:15:41	23:15:51	23:48:34	23:48:44
Nov 6 2017	0:57:09	0:57:20	1:30:02	1:30:13	0:57:09	0:57:20	1:30:02	1:30:13
	2:38:37	2:38:48	3:11:31	3:11:41	2:38:37	2:38:48	3:11:31	3:11:41
	4:20:06	4:20:16	4:53:00	4:53:10	4:20:06	4:20:16	4:52:59	4:53:10
	6:01:34	6:01:45	6:34:28	6:34:38	6:01:34	6:01:45	6:34:28	6:34:38
	7:43:03	7:43:13	8:15:56	8:16:07	7:43:03	7:43:13	8:15:56	8:16:07
	9:24:31	9:24:42	9:57:25	9:57:35	9:24:31	9:24:42	9:57:25	9:57:35
	11:06:00	11:06:10	11:38:53	11:39:04	11:06:00	11:06:10	11:38:53	11:39:04
	12:47:28	12:47:38	13:20:21	13:20:32	12:47:28	12:47:38	13:20:21	13:20:32
	14:28:56	14:29:07	15:01:50	15:02:00	14:28:56	14:29:07	15:01:50	15:02:00
	16:10:25	16:10:35	16:43:18	16:43:29	16:10:25	16:10:35	16:43:18	16:43:29
	17:51:53	17:52:04	18:24:47	18:24:57	17:51:53	17:52:04	18:24:47	18:24:57
	19:33:22	19:33:32	20:06:15	20:06:26	19:33:22	19:33:32	20:06:15	20:06:26
	21:14:50	21:15:01	21:47:44	21:47:54	21:14:50	21:15:01	21:47:44	21:47:54

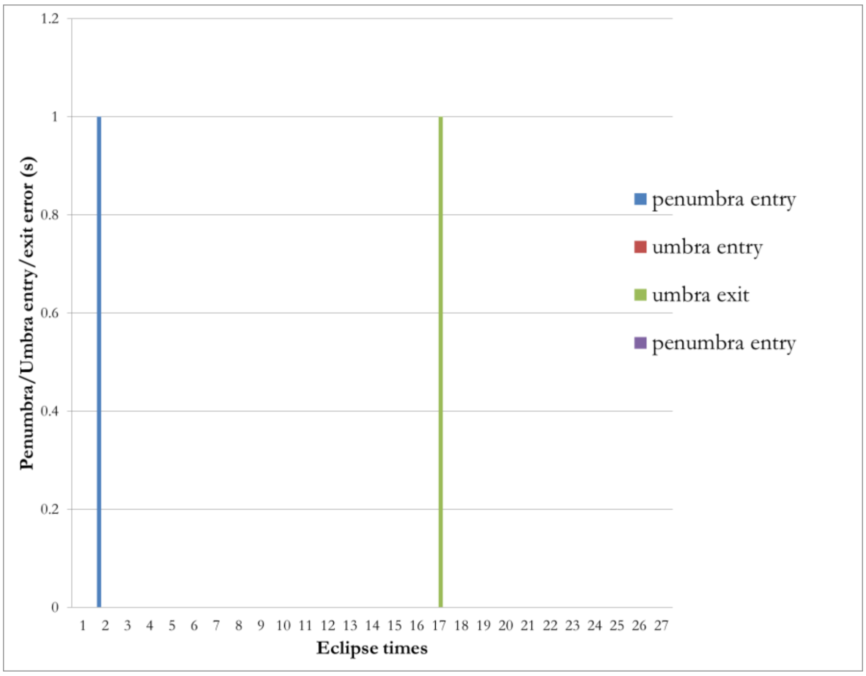

Fig. 16. Relative difference of penumbra and umbra entry/exit with respect to Quartz.

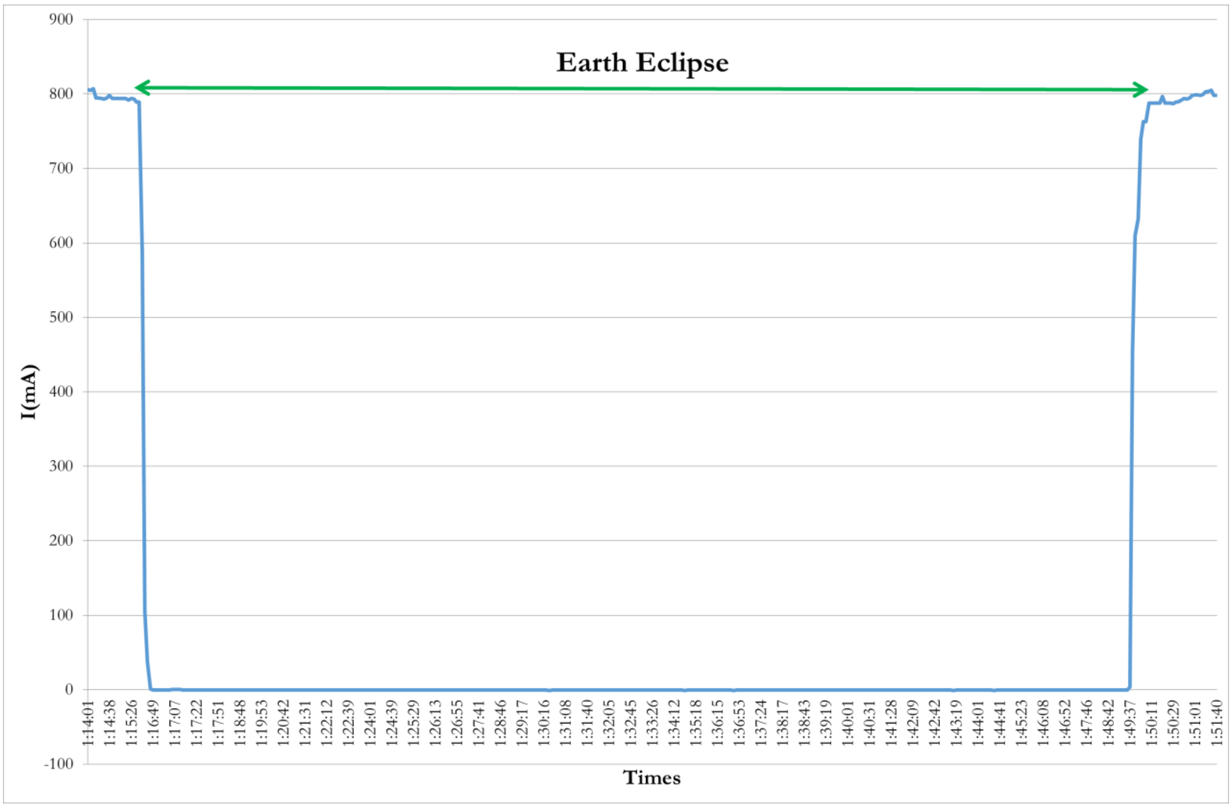

Fig. 17. Charge current evolution of the first Earth Eclipse on Nov 5 2017.

5. Operation time

The comparisons of processing times of both orbit determination and event prediction modules by Quartz and EMERALD, which are collected by 4 operators who have experience to operate FDS, are presented in Fig. 18 and Fig. 19. The results indicate that the overall processing times of Quartz are extremely higher than EMERALD. Especially in event prediction modules, Quartz requires the processing time consumption longer around 5-18 times than EMERALD. This investigation presents that the effectiveness and performance of the EMERALD are improved significantly. Then, Fig. 20 shows the GUI of orbit determination and event prediction modules.

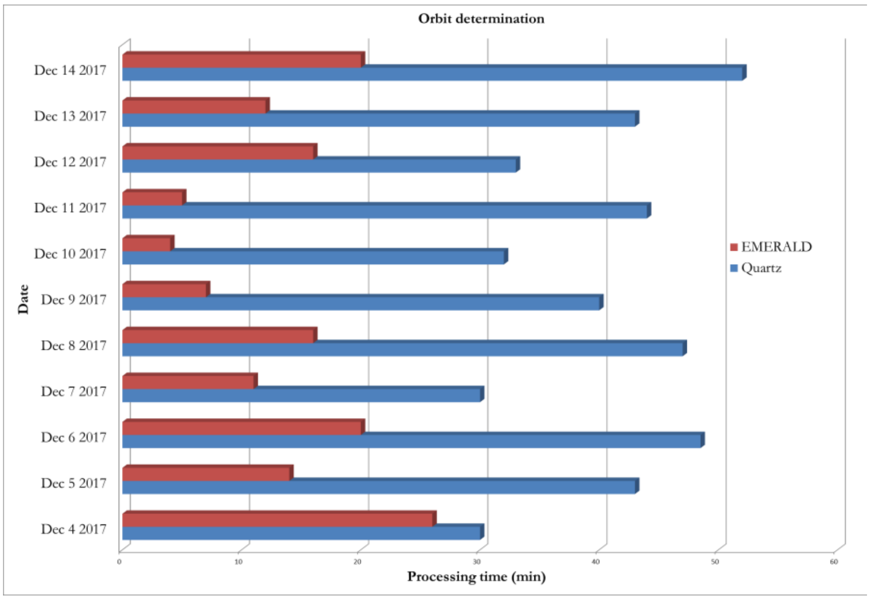

Fig. 18. Comparison the processing time of orbit determination module between Quartz and EMERALD.

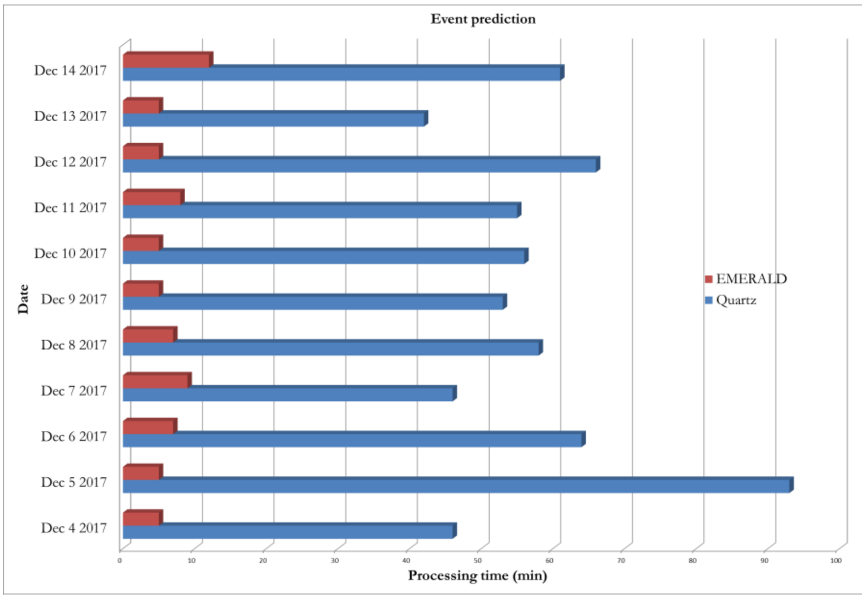

Fig. 19. Comparison the processing time of event prediction module between Quartz and EMERALD.

20171228_034326_Determined(1)

Orbit ID : 910

Epoch : 2017/12/28 03:43:26.112

Px : -2036.9163195452 Py : -6085.8808560315 Pz : 3268.2722691254

Vx : -2.2636705203592 Vy : -2.7605148404875 Vz : -6.5291747080053

START: 2017/12/28 03:43:26.112

END: 2017/12/28 03:43:26.112

```
EMERALD : Orbit Determination Algorithm [2018/01/22 04:42:35.690]

>> System
  Main : Emerald --- Version : -1.0
  Module : Orbit Determination Algorithm --- Version : -1.0
  Satellite : THEOS

>> Configuration :
  Load : Orbit Init --- Format Version : -1
```

a)

20171228_034326_Determined(1)

Epoch : 2017/12/28 03:43:26.112

Px : -2036.9163195452 Py : -6085.8808560315 Pz : 3268.2722691254

Vx : -2.2636705203592 Vy : -2.7605148404875 Vz : -6.5291747080053

START: 2017/12/28 03:43:26.112

END: 2017/12/28 03:43:26.112

Time step (s): 600

● SK Control Windows
○ Eclipses

```
EMERALD : Event Prediction [2018/01/22 04:44:28.447]

>> System
  Main : Emerald --- Version : -1.0
  Module : Event Prediction --- Version : -1.0
  Satellite : THEOS

>> Configuration :
  Load : Orbit Init --- Format Version : -1
```

b)

Fig. 20. GUI a) orbit determination b) event prediction.

6. Conclusion

In this paper, we present the architecture design of EMERALD that consists of five main modules: orbit determination, event prediction, orbit control maneuver, de-orbit simulation and collision risk assessment. The approaches of both orbit determination and event prediction modules implemented for analyzing and performing Thaichote mission are presented in this paper. The analyzed results (orbit determination, orbit prediction, pass schedule and Earth eclipse) of both modules provide the high accuracy of essential mission information by comparing with the mission results. The operation time consumption of EMERALD is significantly faster than Quartz. Future research will thus be focused on full autonomous mission operations, which the system can automatically retrieve GPS data and process mission operation. In addition, the visualization and real-time monitoring tool, which is capable of monitoring a real-time position of a satellite, orbit parameters, mission status and collision risk assessment, will be developed and integrated with EMERALD. The flexible model, which allows a spacecraft shape to be deformed or changed, will be implemented in EMERALD to enhance a propagation accuracy [10, 11].

Acknowledgement

This work was funded by Geo-Informatics and Space Technology Development Agency (Public Organization): GISTDA.

References

[1] H. K. Kuga, P. R. Prasad, and V. Carrara, "Flight dynamics analysis and operational support for CBERS," *Journal of the Brazilian Society of Mechanical Sciences*, vol. 21, pp. 506-513, 1999.
[2] B. S. Lee, Y. Hwang, H. Y. Kim, and J. Kim, "Design and implementation of the flight dynamics system for COMS satellite mission operation," *Acta Astronautica*, vol. 68, pp. 1292-1306, 2011.
[3] M. Aorpimai, P. Navakitkanok, and S. Jantarang. "Automated flight dynamics system for thaichotes satellite operation," in 2*nd IAA Conference on Dynamics and Control of Space System*, 2014, Rome, Italy.
[4] S. Channumsin, P. Udomthanatheera, C. Kositratpatcharasuk, and M. Aorpimai, "Development of an orbital trajectory analysis tool," Engineering Journal, vol. 21, no. 7, pp. 123-139, 2017.
[5] M. Aorpimai and P. Navakitkanok, "Orbit control manoeuvre strategy for post-mission de-orbiting of a low-earth-orbit satellite," *Applied Mechanics and Materials*, vol. 781, pp. 495-499, 2015.
[6] *IADC Space debris mitigation guidelines*, Inter-Agency Space Debris Coordination Committee, Sep. 2007.
[7] J. Stoer and R. Bulirsch, *Introduction to Numerical Analysis*. New York: Springer-Verlag, 1980.
[8] D. D. Pavlis, S. Luo, P. Dahiroc, J. J. McCarthy, and S. B. Luthke, *GEODYN-II Operations Manual*. Greenbelt, Maryland: NASA GSFC, 1998.
[9] C. A. Jablonski, "Application of semianalytic satellite theory to maneuver planning," M.S. thesis, Department of Aeronautics and Astronautics, Massachusetts Institute of Technology, 1991, pp. 143-149.
[10] S. Channumsin, S. Romyen, K. Puttasuwan, and S. Jaturut, "Autonomous systems of real-time monitoring and satellite mission analysis tool," in 69*th International Astronautical Congress 2018*, Berman, Gernany, October 2018.
[11] S. Channumsin, M. Ceriotti, G. Radice, and I. Watson, "Experimental validation of damping properties and solar pressure effects on flexible, high area-to-mass ratio debris model," *Acta Astronautica*, vol. 138, pp. 129-144, 2017.